Satellites and resonant satellites in the photoionization of atomic Cu

J. C. Liu, Z. W. Liu,* and Hugh P. Kelly
Department of Physics, University of Virginia, Charlottesville, Virginia 22901
(Received 23 May 1994)

Many-body perturbation theory has been used to calculate photoionization cross sections with excitations ($3d^{10}4s \rightarrow 3d^9 5skl$, $3d^9 4pkl$, $3d^8 4s^2 kl$, $3d^8 4s 5skl$, and $3d^8 4s 4dkl$) of atomic copper from the single-ionization threshold 7.7–120.0 eV. Resonance structures due to both one-electron excitations ($3p \rightarrow nl$ and $3d \rightarrow nl$) and two-electron excitations ($3d^{10}4s \rightarrow 3d^9 5snl$ and $3d^9 4pnl$) are included. The large nonresonant photoionizations (satellites) leaving the ion in $3d^9 5s$ and $3d^9 4p$ final states are found. The resonant satellites in the region of the $3p$ threshold are the enhanced resonances in the Cu^+ $3d^8 4s^2$ via a super-Coster-Kronig (SCK) transition, and the resonant satellites between 80 and 90 eV in the experiment are the enhanced resonances in the Cu^+ $3d^8 4s 5s$ and $3d^8 4s 4d$ due to SCK decay. The total cross section is in good agreement with the experimental value.

PACS number(s): 32.80.Fb

I. INTRODUCTION

The study of satellite spectra of atoms, which represent cross sections for photoionization with excitation (PIE), has remained an active field of research due to its importance in revealing effects of electron correlations. The photoionization spectrum of atomic copper is an interesting case. The main line of photoionization of Cu is $3d \rightarrow kf, kp$, which is the spectra of the transition metals. However, the resonance structures of Cu and transition metals are different. The strong resonances of atomic Fe, Co, and Ni are produced by $3p \rightarrow 3d$ excitation and a consequent super-Coster-Kronig (SCK) decay [1–7]. In Cu, the $3d$ subshell is full and a weaker $3p \rightarrow 4s$ transition produces a shakeup satellite structure.

In 1979, Iwan, Himpsel, and Eastman observed PIE for Cu [8] which had a resonant behavior similar to that of the satellite previously reported for Ni [1] in 1979. Later they obtained photoionization energy distribution curves in Cu phthalayanine [9] in 1980. Chandesris *et al.* [10] reported the observation of a resonant photoionization line in atomic Cu (Cu vapor) in 1981. Bruhn *et al.* [11] also obtained the photoionization of atomic Cu in the photon energy range 65–90 eV in 1982. The state $3d^8 4s^2[^1G, ^3F, ^1D]$ satellite lines are resonantly enhanced at the energy 73.4 eV of the PIE transition $3p^6 3d^{10}4s \rightarrow 3p^5 3d^{10}4s^2$. They also reported some resonant satellite lines between 80 and 90 eV in their experiment, but did not interpret these lines to belong to the PIE process of the transitions $3p^6 3d^{10}4s \rightarrow 3p^5 3d^8[^1G, ^3F, ^1D]4s 5skl$ and $3p^6 3d^{10}4s \rightarrow 3p^5 3d^8[^1G, ^3F, ^1D]4s 4dkl$.

In theory, Davis and Feldkamp [12] presented a new mechanism for the resonance near the $3p$ threshold in photoionization associated with the two-hole bound state in metals such as Cu and Zn in 1980. The old mechanisms for Ni, which require an empty d state [3,12], could not explain the resonance satellite in Cu. Girvin and Penn [13] analyzed this model using perturbation theory. Davis and Feldkamp extended the formal theory of the interaction of many discrete states with many continua to photoionization and applied the formalism to models which illustrate various aspects of resonant photoionization [14]. They calculated the photoionization of Cu in the region of the $3p$ threshold and used the Fano formalism to treat the resonances and autoionization aspects of the problems [15]. The resonances of excitation $3d^8 4s^2$ due to the SCK decay were calculated in the $3p$ threshold, and the comparatively large nonresonant photoionization due to the excitation $3d^9 4p$ was evaluated numerically.

However, in previous theoretical work, the PIE nonresonant cross section of $3d^9 4p$ was evaluated but not calculated in detail and another large PIE nonresonant cross section of $3d^9 5s$ was neglected. Besides the resonance structure of a PIE transition $3p^6 3d^{10}4s \rightarrow 3p^6 3d^8[^1G, ^3F, ^1D]4s^2 kl$ in the region of $3p$, the experiment also found some resonance structures between 80 and 90 eV, but these lines due to the PIE process of the transitions $3p^6 3d^{10}4s \rightarrow 3p^6 3d^8[^1G, ^3F, ^1D]4s 5skl$ and $3p^6 3d^{10}4s \rightarrow 3p^6 3d^8[^1G, ^3F, ^1D]4s 4dkl$ were not studied in theory. Therefore, there is a need to study the whole energy region and to include all main PIE processes.

Many-body perturbation theory (MBPT) was used to calculate the resonant photoionizations involving the SCK transition, but only for single photoionization of Mn by Garvin *et al.* [16] and Cr by Chang [17], respectively. Also, previous MBPT calculations of photoionization with excitations were carried out for atoms such as Ca^+ [18], Mn [19], and Ar [20] by Kelly and co-workers.

In this paper, applications of MBPT have been extended to photoionization cross sections and resonance structures of PIE processes for open-shell atom Cu. We present a detailed calculation of five PIE processes as follows:

PIE(1): $3p^6 3d^{10}4s \rightarrow 3p^6 3d^9 5skl$,

PIE(2): $3p^6 3d^{10}4s \rightarrow 3p^6 3d^9 4pkl$,

PIE(3): $3p^6 3d^{10}4s \rightarrow 3p^6 3d^8 4s^2 kl$,

*Present address: Department of Physics, University of Notre Dame, Notre Dame, Indiana 46556.

PIE(4): $3p^6 3d^{10} 4s \rightarrow 3p^5 3d^8 4s 5skl$,

PIE(5): $3p^6 3d^{10} 4s \rightarrow 3p^5 3d^8 4s 4dkl$.

Section II includes the theoretical details of our method. Our results are presented in Sec. III, and our discussions and conclusions are given in Sec. IV.

II. THEORY AND METHOD

In this paper, we use the electric-dipole approximation for absorption of electromagnetic radiation and we neglect spin-orbit effects. Atomic units are used throughout the paper.

The photoionization cross section in dipole approximation is given by

$$\sigma(\omega)=\frac{4\pi\omega}{c}\mathrm{Im}\alpha(\omega) , \tag{1}$$

where $\mathrm{Im}\alpha(\omega)$ is the imaginary part of the frequency-dependent dipole polarizability [22,23]. The MBPT expansion for $\alpha(\omega)$ can be derived [24–26] for an atom.

When the atom is exposed to the external electromagnetic radiation field $F_z\cos\omega t$, the resulting interaction is given in the dipole approximation by

$$V_{\mathrm{ext}}=F\cos\omega t\sum_i^N z_i . \tag{2}$$

Using time-dependent perturbation theory, $\mathrm{Im}\alpha(\omega)$ is given in terms of dipole matrix elements and matrix elements of the correlation interaction. The length form of the many-body dipole matrix element is

$$Z_l=\left\langle\Psi_f\left|\sum_i^N z_i\right|\Psi_0\right\rangle \tag{3}$$

and the velocity form is

$$Z_v=(E_0-E_f)^{-1}\left\langle\Psi_f\left|\sum_i^N\frac{d}{dz_i}\right|\Psi_0\right\rangle , \tag{4}$$

where Ψ_0 and Ψ_f are exact many-electron initial and final states, respectively, and E_0 and E_f are energy eigenvalues corresponding to Ψ_0 and Ψ_f.

By use of MBPT, the matrix element $Z_l(Z_v)$ is obtained in finite series of open diagrams which have one dipole interaction and any number of interactions with the electron-correlation perturbation and leading to the final state [25]. In Figs. 1–4 we present the diagrams in our calculation for single photoionization and the PIE process for Cu. The symbols p and q represent core orbitals, r represents a bound excited orbital, n represents a series of excited orbitals, k represents a continuum orbital, and ϵ represents both excited and continuum orbitals. The exchange diagrams are not shown, but are understood to be included. We show the diagram of single photoionization ($p\rightarrow k$) in Fig. 1 which include interactions between different single excited-final-state channels. We give the diagrams of single photoionization ($p\rightarrow k$) in Fig. 2 which include interactions between $p\rightarrow k$ and $p,q\rightarrow r,k$. The transition $p\rightarrow k$ is described by the lowest-order diagram Fig. 1(a), the first ground-state correlation diagram Fig. 1(b), the first final-state correlation diagram Fig. 1(c), the random-phase approximation (RPA) diagrams Figs. 1(d)–1(i), the Breuckner-orbital correction (BO) diagrams Figs. 2(a)–2(d), and the structure-radiation-type (SR) diagrams Figs. 2(e)–2(j). In Fig. 3 we show the diagrams for

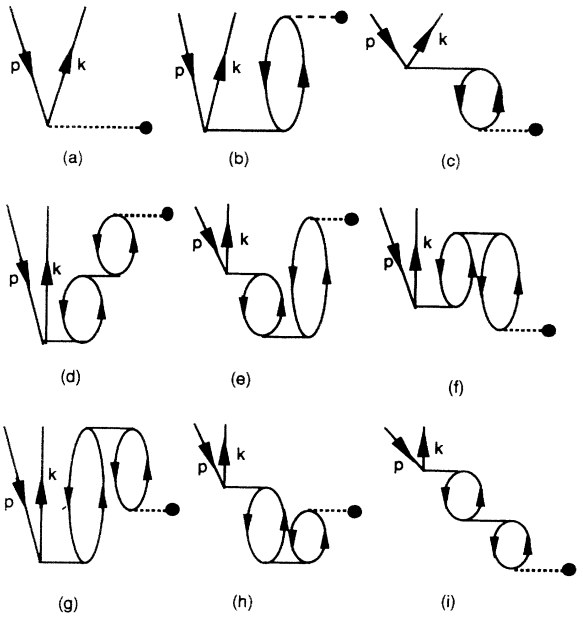

FIG. 1. Diagrams of single photoionization $p\rightarrow k$ which include interactions with the transition $p'\rightarrow k'$. Dashed lines ending with a solid dot indicate matrix elements of Z. Solid lines represent Coulomb interaction.

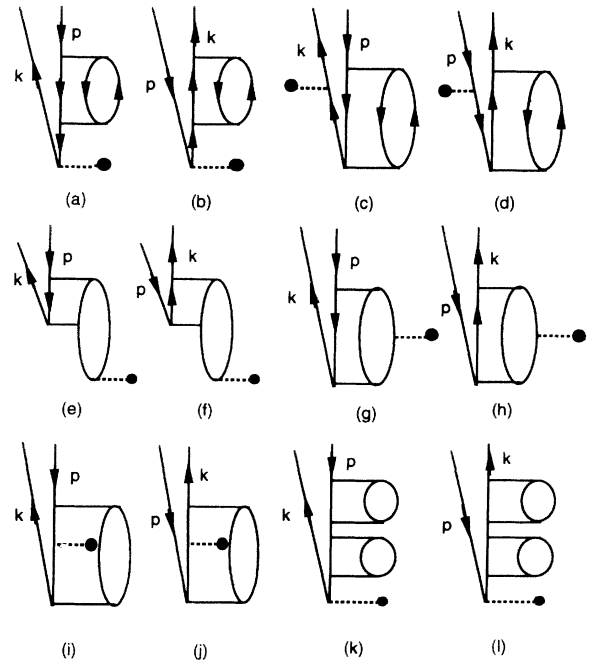

FIG. 2. Diagrams of single photoionization $p\rightarrow k$ which include interactions with PIE transitions $p,q\rightarrow r,k$. Dashed lines ending with a solid dot indicate matrix elements of Z. Solid lines represent Coulomb interaction.

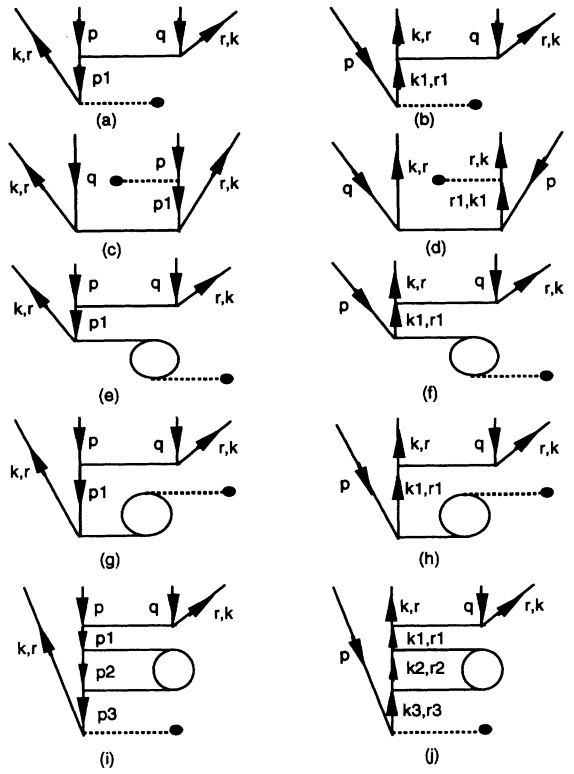

FIG. 3. Diagrams of nonresonant satellites $p,q \rightarrow r,k$. Dashed lines ending with a solid dot indicate matrix elements of Z. Solid lines represent Coulomb interaction.

nonresonant satellites [PIE(1) and PIE(2)]. The transitions $p,q \rightarrow r,k$ of photoionization with excitation (r) include the lowest-order diagrams Figs. 3(a)–3(d) and the correlation diagrams Figs. 3(e)–3(h). Since preliminary calculations indicate that resonant satellites [PIE(3), PIE(5)] have enhanced resonance structures due to SCK decay, we calculate these transitions and concentrate on the diagrams in Fig. 4 which have the dominant contribution to this kind of resonance. We notice that SCK decay is one of the Auger contributions. We include the Auger contribution diagrams in our coupled-equation method [21] and calculated all-order approximations for these diagrams.

In order to calculate the diagrams of Figs. 1–4 we calculate a complete set of radial states for each value of orbital angular momentum which is used. These states

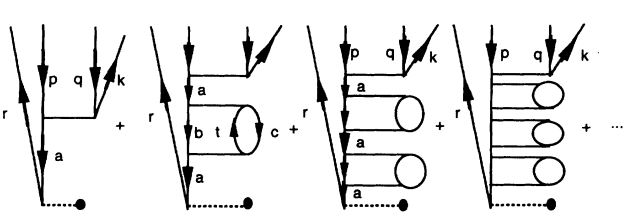

FIG. 4. Diagrams of resonant satellites $p,q \rightarrow r,k$. Dashed lines ending with a solid dot indicate matrix elements of Z. Solid lines represent Coulomb interaction.

satisfy the one-particle equation

$$[\nabla^2/2 - Z/r + V(r)]\phi_i = \varepsilon_i \phi_i \ . \tag{5}$$

The general form of potential for single-particle states used in the evaluation of diagrams is [27]

$$V = R - (1-P)\Omega(1-P) \ , \tag{6}$$

where P is the projection operator given by

$$P = \sum_i |i\rangle\langle i| \ , \tag{7}$$

where i runs over occupied ground-state orbitals. In Eq. (6) R is the Hartree-Fock (HF) potential for ground-state orbitals and Ω is a Hermitian operator chosen to give a physically appropriate potential for excited states.

The ground-state radial orbitals in our basis were calculated by using Froese Fischer's computer program MCHF77 [28]. The radial $4s$ orbital of the excitation state $3p^6 3d^8 4s^2$ was used by the same orbital as the ground-state $4s$ orbital, since the ground state $4s$ is considered as a valence orbital of the frozen ionic core $(3p^6 3d^{10})$. The radial $5s$ and $4p$ orbitals of the excitation states $3p^6 3d^9 5s\epsilon l$ and $3p^6 3d^9 4p\epsilon l$ were calculated in the self-consistent HF approximation of the ionic cores $3p^6 3d^9 5s$ and $3p^6 3d^9 4p$. The radial $5s$ and $4d$ orbitals of the excitation states $3p^6 3d^8 4s 5s\epsilon l$ and $3p^6 3d^8 4s 4d\epsilon l$ were calculated in the self-consistent HF approximation of the ionic cores $3p^6 3d^8 4s 5s$ and $3p^6 3d^8 4s 4d$. The radial orbitals ϵl in the excitations $3p^6 3d^9 5s\epsilon l$ and $3p^6 3d^9 4p\epsilon l$ were calculated in the potential appropriate to the ionic cores $3d^9 5s$ and $3d^9 4p$, respectively. The radial orbitals ϵl in the excitations $3d^8 4s^2 \epsilon l$, $3d^8 4s 5s$, and $3d^8 4s 4d$ were calculated in HF potentials appropriate to the ionic cores $3p^6 3d^8 4s^2$, $3p^6 3d^8 4s 5s$, and $3p^6 3d^8 4s 4d$, respectively. All the orbitals, which are represented by ϵl, are calculated under the V^{N-1} potential defined by Eq. (6).

We have two sets of final-state channels in our calculation corresponding to the two kinds of PIE processes. One of them is for the ion in the levels $3p^6 3d^9 4p$ and $3p^6 3d^9 5s$ [PIE(1) and PIE(2), respectively] and is given in Table I. The other one is for the ion in the levels $3p^6 3d^8 4s^2$, $3p^6 3d^8 4s 5s$, and $3p^6 3d^8 4s 4d$ [PIE(1), PIE(2), and PIE(3), respectively] and is given in Table II. Our coupled-equations method is to account for interactions between channels in the final states. When the ionic core $3d^9$ is as in PIE(1) and PIE(2), PIE processes have large effects on the nonresonant cross section. When the ionic core $3d^8 4s$ is as in PIE(3)–PIE(5), PIE processes give a large contribution only for the enhanced resonance structures due to SCK decay. In our calculations, we use three different kinds of total final channel interactions in the coupled-equations method as follows: (a) 5-channel interactions (single photoionization), (b) 17-channel interactions [single photoionization and PIE(1) and PIE(2)], and (c) 17-channel interactions [single photoionization and PIE(3)–PIE(5)].

Tables I and II list the final-state channels in LS coupling, along with photoionization threshold energies. We use the ΔSCF energies (where SCF denotes self-consistent

TABLE I. Channels and threshold energies.

No.	Channels and states	Threshold energies (a.u.)
1	$3p^6 3d^{10}\epsilon p$	0.283 938
2	$3p^5 3d^{10}4s\epsilon s$	3.262 78
4	$3p^5 3d^{10}4s\epsilon d$	3.262 78
4	$3p^6 3d^9 4s\epsilon p$	0.403 608
5	$3p^6 3d^9 4s\epsilon f$	0.403 608
6	$3p^6 3d^9 5s[^1D]\epsilon s1$	0.786 825
7	$3p^6 3d^9 5s[^3D]\epsilon s2$	0.779 772
8	$3p^6 3d^9 5s[^1D]\epsilon d1$	0.786 825
9	$3p^6 3d^9 5s[^3D]\epsilon d2$	0.779 772
10	$3p^6 3d^9 4p[^1P]\epsilon s1$	0.619 266
11	$3p^6 3d^9 4p[^3P]\epsilon s2$	0.592 532
12	$3p^6 3d^9 4p[^1P]\epsilon d1$	0.619 266
13	$3p^6 3d^9 4p[^3P]\epsilon d2$	0.592 532
14	$3p^6 3d^9 4p[^1D]\epsilon d3$	0.616 352
15	$3p^6 3d^9 4p[^3D]\epsilon d4$	0.600 114
16	$3p^6 3d^9 4p[^1F]\epsilon d5$	0.619 373
17	$3p^6 3d^9 4p[^3F]\epsilon d6$	0.608 876

field) for channels $3p^5 3d^{10}4s\epsilon l$, $3p^6 3d^8 4s5s\epsilon l$, and $3p^6 3d^8 4s4d\epsilon l$, but use experimental threshold energies [31] for all other final-state channels. The symbol ϵ in Tables I and II is either a continuum orbital k or a bound excited orbital n. Thus the PIE final states in Tables I and II also include double-electron excitation when the symbol ϵ represents a bound excited orbital, and our calculation can show both single-electron and double-electron resonance structures.

III. RESULTS

A. Nonresonant satellites

We present results in both the lowest-order approximation and the approximation including higher-order correlations for the sum of cross sections of the PIE processes

TABLE II. Channels and threshold energies.

No.	Channels and states	Threshold energies (a.u.)
1	$3p^6 3d^{10}\epsilon p$	0.283 938
2	$3p^5 3d^{10}4s\epsilon s$	3.262 78
3	$3p^5 3d^{10}4s^2$	2.952 97
4	$3p^5 3d^{10}4s5s$	3.208 49
5	$3p^5 3d^{10}4s\epsilon d$	3.262 78
6	$3p^5 3d^{10}4s4d$	3.194 56
7	$3p^6 3d^9 4s\epsilon p$	0.403 608
8	$3p^6 3d^9 4s\epsilon f$	0.403 608
9	$3p^6 3d^8[^1G]4s^2\epsilon l1$	0.719 367
10	$3p^6 3d^8[^3F]4s^2\epsilon l2$	0.608 896
11	$3p^6 3d^8[^1D]4s^2\epsilon l3$	0.672 998
12	$3p^6 3d^8[^1G]4s5s\epsilon l1$	1.457 837
13	$3p^6 3d^8[^3F]4s5s\epsilon l2$	1.462 708
14	$3p^6 3d^8[^1D]4s5s\epsilon l3$	1.468 366
15	$3p^6 3d^8[^1G]4s4d\epsilon l1$	1.253 644
16	$3p^6 3d^8[^3F]4s4d\epsilon l2$	1.251 707
17	$3p^6 3d^8[^1D]4s4d\epsilon l3$	1.237 366

$3d,4s \rightarrow 5s,kl$ in Fig. 5 and of the PIE processes $3d,4s \rightarrow 4p,kl$ in Fig. 6. The lowest-order approximation only includes the diagrams of Figs. 3(a)–3(d). The diagrams of Figs. 3(e)–3(h) give corrections for the dipole operator in Figs. 3(a) and 3(b) and improve the agreement of the length and velocity forms considerably. In Fig. 5 we see that the cross section of the PIE processes $3d,4s \rightarrow 5s,kl$ increases rapidly from the threshold energy to 48 eV and then slowly decreases. In Fig. 6 we also see that the cross section of the PIE processes $3d,4s \rightarrow 4p,kl$ decreases rapidly from the threshold energy to 48 eV and then slowly decreases.

We show four different contributions for the transitions $3d,4s \rightarrow 5s,kf$ in Fig. 7 and $3d,4s \rightarrow 4p,kd$ in Fig. 8. Ground-state correlation includes the two ground-state correlation diagrams in Figs. 3(c) and 3(d). The final-state correlations are divided into shake-off, virtual Auger, and knockout. The shakeoff correlation includes the diagrams of Figs. 3(a), 3(e), and 3(g) for the same electrons p and p_1, but the virtual Auger correlation for different electrons p and p_1. Knockout includes the diagrams of Figs. 3(b), 3(f), and 3(h). We notice that substantial contributions are given by shakeoff correlation for the transition $3d,4s \rightarrow 5s,kf$ in Fig. 3, but by the knockout correlation for the transition $3d,4s \rightarrow 4p,kd$ in Fig. 4. We also notice that the contribution of the shakeoff correlation is much stronger than that of the virtual Auger correlation since shakeoff has the Coulomb interaction between the same p and p_1 electron.

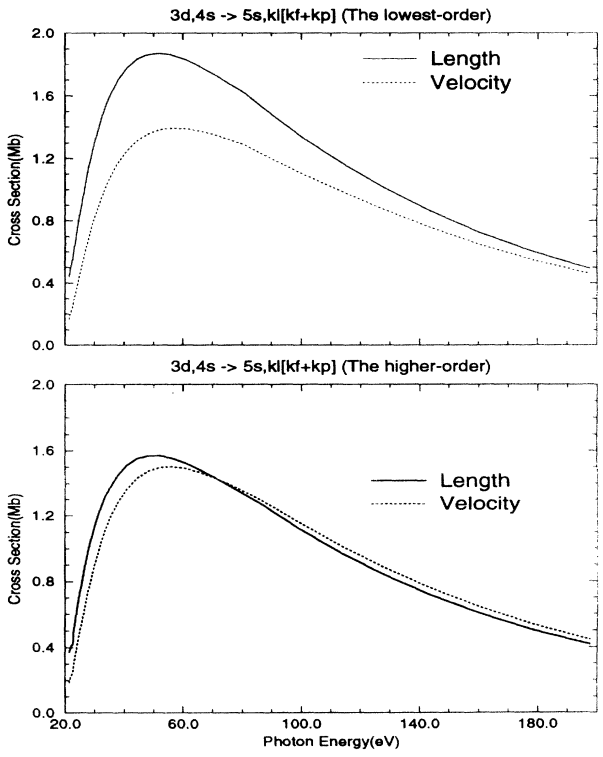

FIG. 5. Cross sections of the PIE processes $3d,4s \rightarrow 5s,kl$ in dipole length and dipole velocity formalism.

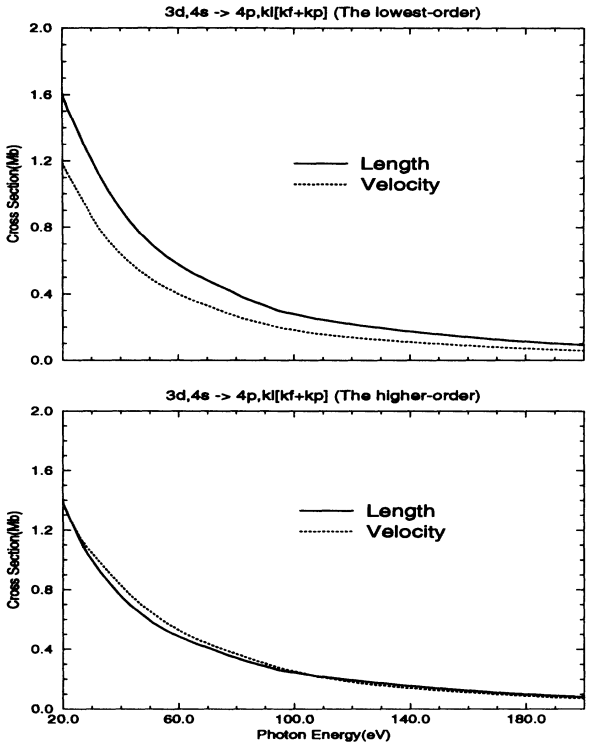

FIG. 6. Cross sections of the PIE processes $3d,4s \rightarrow 4p,kl$ in dipole length and dipole velocity formalism.

B. Single photoionization

We present the cross sections of photoionization ($3d \rightarrow kp + kf$) in velocity form with different higher-order corrections in Fig. 9. The main terms of the second-order correlation are included in our calculation for the transition $3d \rightarrow kl[kp + kf]$. For RPA terms we included all kinds of RPA diagrams [Figs. 1(d)–1(i)]. For BO and SR terms we only included main BO and SR diagrams [Figs. 2(a)–2(j)]. In order to set up the coupled channels in as few transitions as possible, we only included the dominant transitions ($3p \rightarrow kd, 3p \rightarrow ks, 3d \rightarrow kp$, $3d \rightarrow kf$, and $4s \rightarrow kp$) in the RPA correlation, since the contributions from the transitions $1s \rightarrow kl$, $2s \rightarrow kl$, $2p \rightarrow kl$, and $3s \rightarrow kl$ are very small. For the same reason we included only two substantial transitions $3d,4s \rightarrow 5s,kl$ and $4p,kl$ in BO and SR terms. We notice that the cross section is reduced by the second-order correlations of RPA, BO, and SR terms. We also notice that these second-order terms give more correction for cross sections at low energy than at high energy since they give more correction on our wave functions at lower energy region. From photon energies 70.0–83.5 eV there are resonances due to one-electron excitations $3p \rightarrow ns, nd$ ($n = 4, 5, \ldots, 13$). The resonances corresponding to two-electron excitations $3d,4s \rightarrow 5s,nl$ and $4p,nl$ occur between 9.6 and 16.8 eV.

We present our results in Fig. 10 for the cross sections of photoionization ($3d \rightarrow kf$) in various first-order and second-order approximations. We notice that the first-order ground-state correlations give a large contribution to the velocity approximation, but the first-order final-state correlations give a large contribution to the length approximation. The length approximation agrees well with the velocity approximation when both the first-order final-state and ground-state correlations are included. The second-order correlations decrease cross sections in both length and velocity approximations.

We present our results in Fig. 11 for the partial cross sections of photoionization ($3p \rightarrow kd, ks$). We notice that the cross section of $3p$ is much smaller than the cross section of $3d$ and it is not sensitive to the higher-order corrections.

We present our results in Fig. 12 for the partial cross sections of photoionization ($4s \rightarrow kp$) from threshold energy 7.72–100 eV calculated by using three different approximations. We notice that the cross section of $4s$ is much smaller than the cross section of $3d$ and it is affected considerably by the second-order correlations, the same as the $3d$ electron.

C. Resonant satellites

For PIE processes $3d,3d \rightarrow 4s,kl$, $3d,3d \rightarrow 5s,kl$, and $3d,3d \rightarrow 4d,kl$ we have calculated their nonresonant cross sections and enhanced resonance structure. We present results in Fig. 13 for the sum of cross sections of the PIE processes $3d,3d \rightarrow 4s,kl = kf1 + kf2 + kf3$, $3d,3d \rightarrow 5s,kl = kf1 + kf2 + kf3$, and $3d,3d \rightarrow 4d,kl = kf1 + kf2 + kf3$. We find that the satellite line of resonance due to $3p \rightarrow 4s$ from 65 to 78 eV is enhanced in the PIE processes $3d,3d \rightarrow 4s,kl$. We also find that the resonances for $3p \rightarrow 5s$ and $3p \rightarrow 4d$ from 81 to 85 eV are enhanced in the PIE process $3d,3d \rightarrow 5s,kl$ and $3d,3d \rightarrow 4d,kl$, respectively. We do not include the PIE processes $3d,3d \rightarrow 4s,kp$, $5s,kp$, and $4d,4p$ since these transitions give a much smaller contribution than the PIE processes $3d,3d \rightarrow 4s,kf$, $5s,kf$, and $4d,kf$. Compared with resonant satellites, the nonresonant cross sections are small so that we can neglect interactions between them and single photoionization.

We present results in Fig. 14 for the enhanced resonance structure of the transitions $3p \rightarrow 4s, 5s, 4d$ in the PIE processes $3d,3d \rightarrow nl$ $[= 4s, 5s, 4d], kl$. We show the experimental values [11], which give two resonance structures in 65–78 and 81–85 eV. Bruhn *et al.* [11] observed the resonant structures in 81–85 eV, but did not give an explanation about them. We also show the other calculation result of the resonance structure in 65–78 eV [15]. We notice that the results of our calculation are in good agreement with experimental measurements in both 65–78 and 81–85 eV. The PIE final states $3d^8[^1G, ^3F, ^1D]nl'kl$ ($nl' = 4s$, $5s$, or $4d$) are calculated, but the PIE final states $3d^8[^3P, ^1S]nl'kl$ ($nl' = 4s$, $5s$, or $4d$) are negligible. The experimental percentages [11] of the PIE transitions $3d,3d \rightarrow 4s,kl$ are ^1G (63%), ^3F (27%), ^1D (6%), and $^3P + ^1S$ (4%). In Fig. 14 our calculated percentages of the PIE transitions are ^1G (63%), ^3F (27%), and ^1D (8%) for the PIE processes $3d,3d \rightarrow 4s,kl$ and ^1G(60%), ^3F (32%), and ^1D (6%) for the PIE processes

$3d,3d \rightarrow 5s,kl$ and $4d,kl$.

In Fig. 15 we present our calculated total cross section and the experimental value [6] from 60 to 90 eV. These experimental data are the absorption data of atomic copper. We notice that the results of our calculation are in good agreement with experimental measurements.

IV. DISCUSSION AND CONCLUSION

We have used many-body theory to calculate the photoionization cross sections for copper, leaving Cu^+ in excited-state levels $3d^9 5s, 3d^9 4p, 3d^8 4s^2, 3d^8 4s 5s$, and $3d^8 4s 4d$. Our calculations include resonance structure due to one- and two-electron excitations and are in good agreement with experiment.

The transitions $3d,4s \rightarrow nl[=4p,5s],kl$ are the PIE processes in which $4s$ is excited or ionized. The transitions $3d,3d \rightarrow nl[=4s,5s,4d],kl$ are the PIE processes in which one of two $3d$ electrons is excited and the other one is ionized. We compare the cross sections between the $3d,4s \rightarrow nl[=4p,5s],kl$ transitions in Figs. 5 and 6 and the $3d,3d \rightarrow nl[=4s,5s,4d],kl$ transitions in Fig. 13. We find that $3d^9[4p,5s]kl$ has a much larger nonresonant cross section and $3d^8[4s^2,4s5s,4s4d]kl$ has a small nonresonant cross section with enhanced resonance structures. The reason is that $4s$ is easier to excite or ionize than the $3d$ electron. In our calculations we also notice that there are strong interactions between the channels $3d^9[4p,5s]kl$ and the single photoionization channels such as $3d \rightarrow kl$.

Near threshold our length form does not agree well with the velocity form because our calculations do not include effects of relaxation and polarization.

In Fig. 9 the $3d$ cross section is reduced significantly by including the PIE $3d^9 5skl$ and $3d^9 4pkl$ channels. We interpret this as the loss of flux from the single photoionization $3d \rightarrow kl$ to the PIE $3d^9 5skl$ and $3d^9 4pkl$ channels. In our calculation we find that the flux to $3d^9 5skl$ and $3d^9 4pkl$ should not be neglected since it has the strong Coulomb interaction ($\kappa=0$). In our calculation, we find that the resonance $3p \rightarrow 4s$, $5s$, or $4d$ will not occur if we include the channels of excitation $3d^8 4s^2$, $3d^8 4s 5s$, and

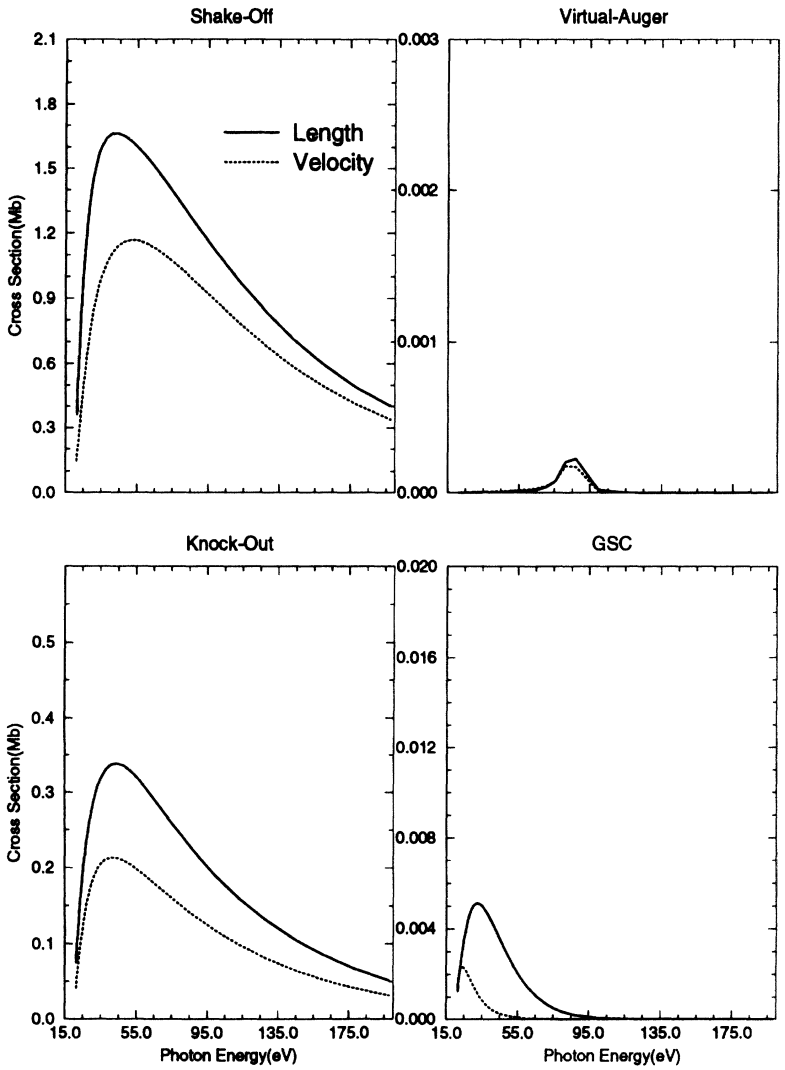

FIG. 7. Four contributions of the diagrams $3d,4s \rightarrow 5s,kf$ in dipole length and dipole velocity formalism.

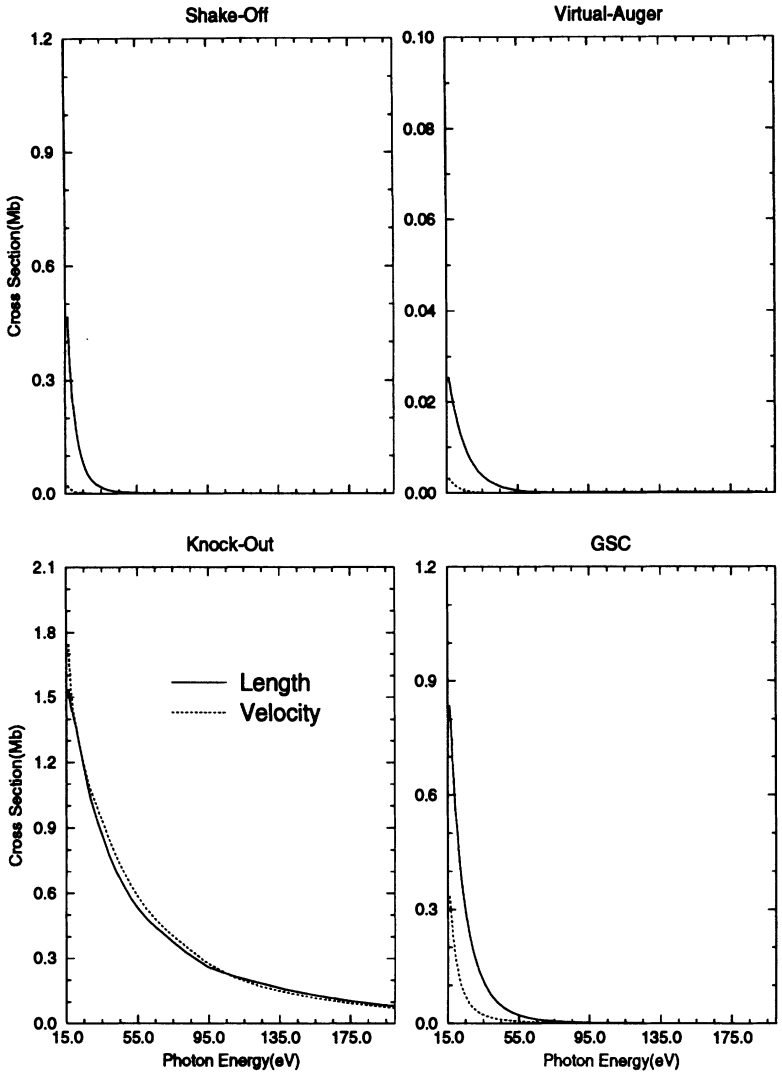

FIG. 8. Four contributions of the diagrams $3d,4s \rightarrow 4p,kd$ in dipole length and dipole velocity formalism.

$3d^8 4s 4d$. We can also interpret this as loss of the resonance $3p \rightarrow 4s$, $5d$, and $4d$ from the transitions $3d \rightarrow kl$ and $4s \rightarrow kp$ to the transitions $3d^8 4s^2 kl$, $3d^8 4s 5skl$, and $3d^8 4s 4dkl$, respectively.

In Fig. 9 we find that RPA and BO diagrams have dominant contributions to the cross section in the second-order correlation. RPA terms include the interaction among the single photoionization transitions $3p \rightarrow kl$, $3d \rightarrow kl$, and $4s \rightarrow kp$. BO terms include the interactions between single photoionizations $3d \rightarrow kl$ and PIE processes $3d,4s \rightarrow nl,kl$. BO terms give contributions at the same level as RPA terms because the transitions $3d,4s \rightarrow 5s,kl$ and $4p,kl$ are at the same level as the transition $3d \rightarrow kp$ and larger than the transitions $4s \rightarrow kp$ and $3p \rightarrow kl$. We note that the SR correlation is much less than the BO correlation. The dominant diagrams for BO terms are Figs. 2(a) and 2(b), and for SR terms they are Figs. 2(e) and 2(f). Comparing the BO term of Fig. 2(a) with the SR term of Fig. 2(e), we find that the virtual electron (p) interacts with a dipole directly for the BO term, but indirectly for the SR term. Comparing the BO

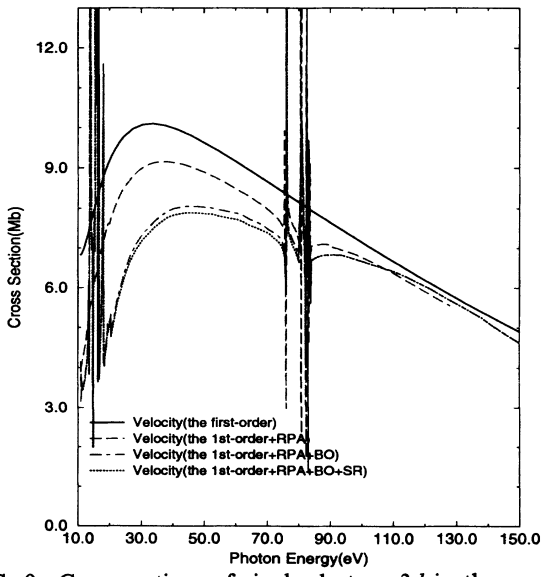

FIG. 9. Cross sections of single-electron $3d$ in the second-order correlations.

term of Fig. 2(b) with the SR term of Fig. 2(f), we find that an ionized electron (k) interacts with a dipole directly for the BO term, but indirectly for the BO term.

There would be a large resonance ($3d \rightarrow 4p$) occurring in the single photoionization ($4s \rightarrow kp$), but we did not find it in the cross section of $4s \rightarrow kp$. This is because the position 6.34 eV of this resonance $3d \rightarrow 4p$ moves below the threshold energy 7.72 eV of $4s$ electron. This hidden resonance, however, enhances the $4s$ cross section at the threshold energy. Since the threshold energy of $3d, 3d \rightarrow 4p, kl$ is 43.2 eV, which is much higher than the resonance position 6.34 eV, we did not calculate the PIE processes $3d, 3d \rightarrow 4p, kl$, although there is a decay via the super-Coster-Kronig transition for $3d \rightarrow 4p$.

The peaks in absorption for the transition metals (Cr, Mn, Fe, Co, etc.) [6,16,17] are asymmetric and broad due to Fano resonances [29], which exist because the excited states $3p^5 3d^{n+1} 4s^2$ from the ground states $3p^6 3d^n 4s^2$ (excitation $3p \rightarrow 3d$) decay via the SCK transition [30] to the final states $3p^6 3d^{n-1} 4s^2 kl$. These final states can be excited directly from the ground states by one-electron transitions. Both the large width and the prominent asymmetry are due to the strength of the SCK matrix elements. In Cu the $3d$ subsell is full and the absorption is due to the $3p \rightarrow 4s$, $5s$, or $4d$ transition. The excited states $3p^5 3d^{10}(4s^2, 4s5s, 4s4d)$ from the ground states $3p^6 3d^{10}(4s, 5s, 4d)$ can decay via the SCK transition to final states $3p^6 3d^8(4s^2, 4s5s, 4s4d)kl$. However, these final states of Cu are photoionization with excitations and are different from the final states of Cr, Mn, and Fe in SCK transitions. The PIE processes $3p^6 3d^8(4s^2, 4s5s, 4s4d)kl$ from ground state are weak because they are involved in two-electron transitions.

The dominant contribution to the enhanced resonances is from the lowest-order diagram of PIE in Fig. 3(a). The energy denominator of this diagram involves an integration over the continuum state, which, through a principal-value integral, has an imaginary part which will

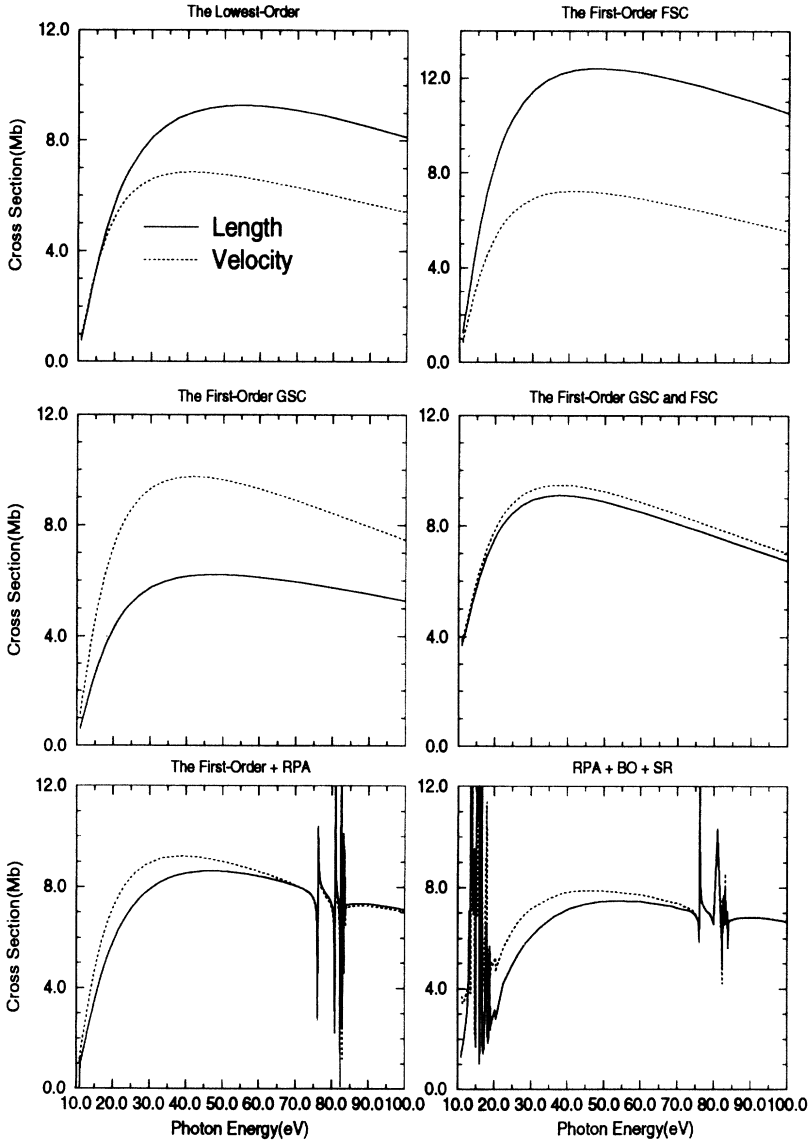

FIG. 10. Cross sections of $3d \rightarrow kf$ in the first- and second-order correlations.

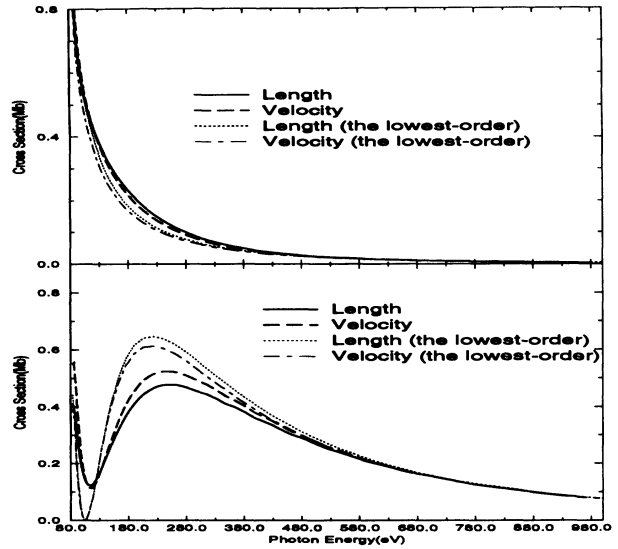

FIG. 11. Cross sections of single-electron $3p$ in dipole length and dipole velocity formalism.

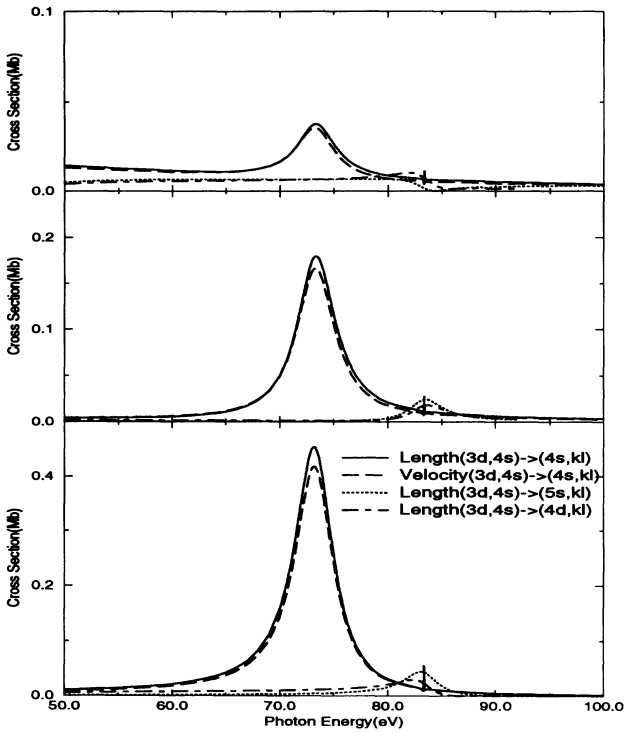

FIG. 13. Photoionization cross section for $3d^{10}4s \rightarrow 3d^{8}4s[4s,5s,4d]kl$ in dipole length and dipole velocity formalism.

contribute to the width of the resonance. A technique used to sum the final-state correlation diagrams to infinite order is used here to treat the all-order Auger contribution diagrams. A graphic representation is shown in Fig. 16. The imaginary part $\mathcal{J}$ can be written explicitly as

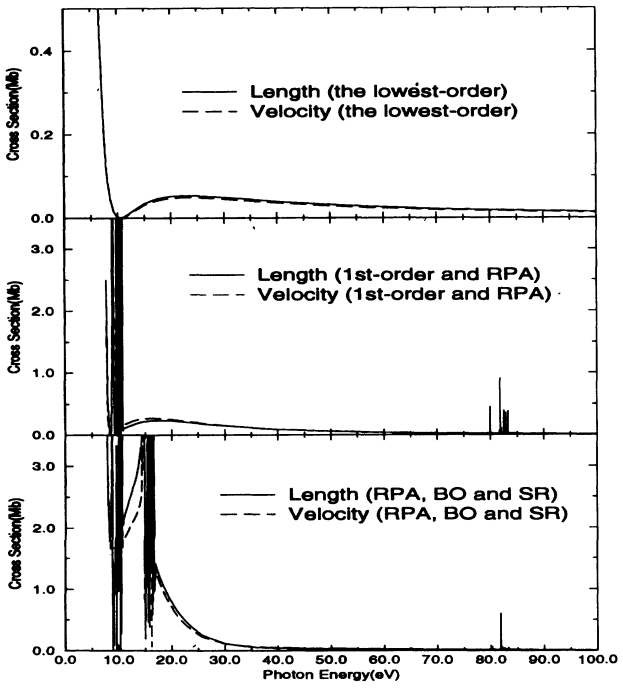

FIG. 12. Cross sections of single-electron $4s$ in dipole length and dipole velocity formalism.

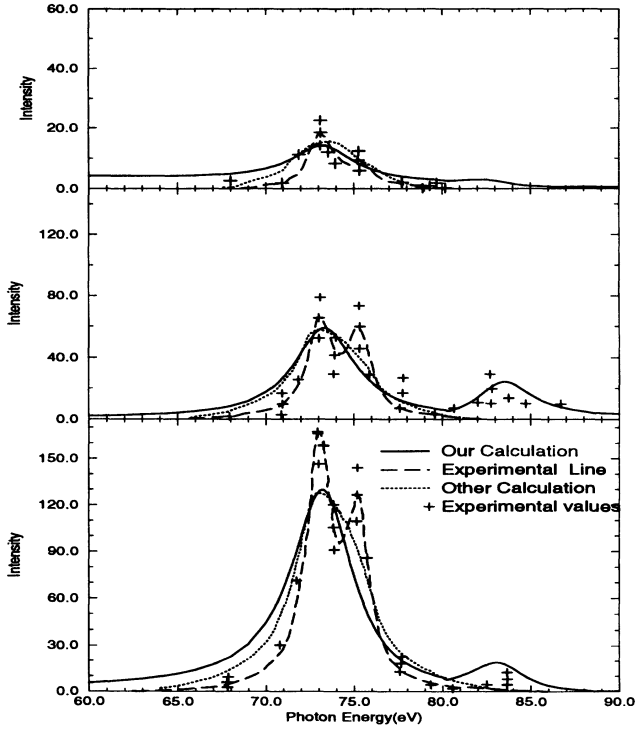

FIG. 14. Resonant structure of $3p \rightarrow [4s,5s,4d]$ for PIE processes $3d^{10}4s \rightarrow 3d^{8}4s[4s,5s,4d]kl$. The solid line represents our calculations. The dashed line represents the calculation by Davis and Feldkamp [15]. The long-dashed line represents the experiment by Brunh *et al.* [11].

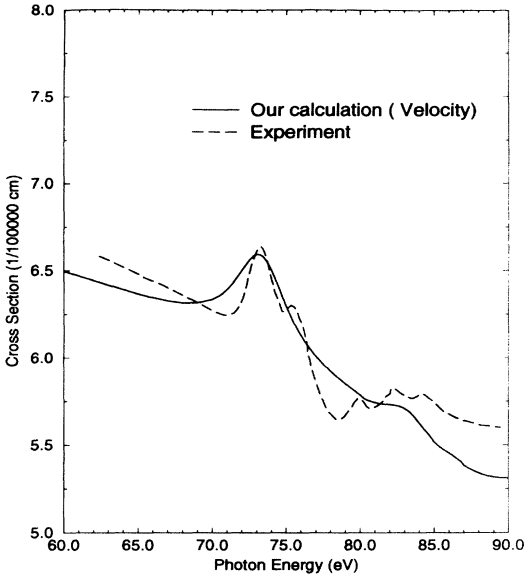

FIG. 15. Total cross section between 60 and 90 eV. The solid line represents our calculations. The dotted line represents the experiment by Brunh, Sonntag, and Wolff [6].

$$\mathcal{J}=\left[\frac{2}{\pi}\right](-i\pi)\int dk_t \frac{|\langle v\rangle_{ctab}\langle v\rangle_{abct}|^2}{\varepsilon_a-\varepsilon_r+\omega} \times\delta\left[\varepsilon_c+\varepsilon_b-\varepsilon_\tau-\frac{k_t^2}{2}+\omega\right] =i\frac{\Gamma/2}{\varepsilon_a-\varepsilon_\tau+\omega}\ , \tag{8}$$

where

$$\frac{\Gamma}{2}=-\frac{2}{k}|\langle v\rangle_{ctab}\langle v\rangle_{abct}|^2 \tag{9}$$

with

$$k=\sqrt{2(\varepsilon_c+\varepsilon_b-\varepsilon_r+\omega)}\ . \tag{10}$$

It can be seen that $\Gamma/2$ is ω dependent. At the energy of resonance $\omega=\varepsilon_a-\varepsilon_r$, k can be expressed as

$$k=\sqrt{2(\varepsilon_c+\varepsilon_b-\varepsilon_a)}\ . \tag{11}$$

We obtain the widths of $3p\rightarrow 4s,5s,4d$ as 3.53, 3.24, and 3.22 eV, respectively. Most of the widths come from SCK transitions to $3d^8 4s^2$, $3d^8 4s\,5s$, and $3d^8 4s\,4d$. In Fig. 14 the two $3p$ spin-orbit components are separated in the experimental data [11], which are represented by the superposition of two Lorentzian curves positioned at the energies 73.15 and 75.4 eV of the $3p^6 3d^{10} 4s \rightarrow 3p^5(^2P_{1/2},{}^2P_{3/2})3d^{10}4s^2$ transitions. Our calculated linewidth is about twice the experiment value [11] since the spin-orbit splitting is not included in the theoretical curves.

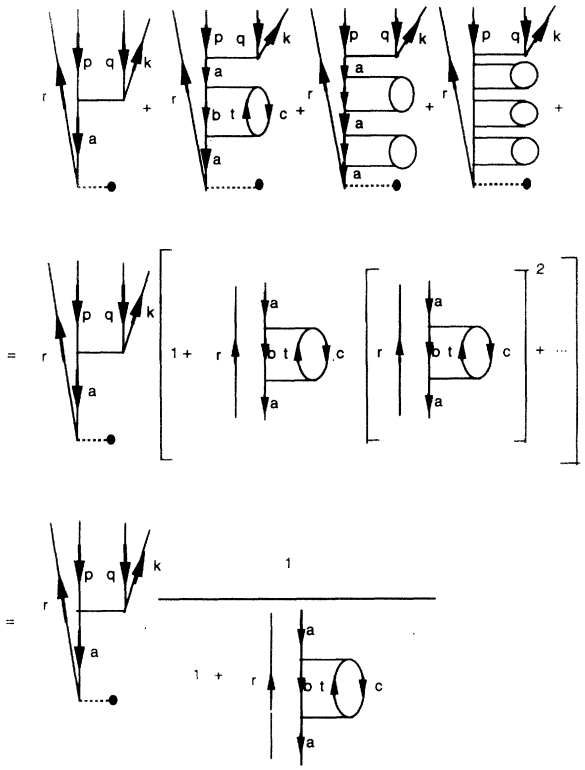

FIG. 16. Summation of the Auger contribution diagrams.

In summary we have found many-body perturbation theory to be useful in calculating cross sections of photoionization with excitations for the open-shell atom Cu. We notice that the large nonresonant cross section comes from the photoionization with excitation ($3d^{10}4s \rightarrow 3d^9 5skl, 3d^9 4pkl$). We find that the enhanced resonances in the excitation states $3d^8 4s^2, 4s\,5s, 4s\,4d$ due to SCK decay occur in the $3p$ threshold for Cu. The total cross section is in reasonable agreement with experimental data. It is desirable to include the spin-orbit interaction in further calculations for PIE processes.

ACKNOWLEDGMENTS

The authors are grateful to the U.S. National Science Foundation for support of this work under Grant No. PHY 90-07883. Most of the calculations were performed on an IBM/RISC6000/540 workstation at the University of Virginia. The authors would also like to thank Walter Johnson, Jesses Chang, James Boyle, and Cheng Pan for helpful discussion.

[1] C. Guillot, Y. Ballu, J. Paigne, J. Lecante, K. P. Jain, P. Thiry, R. Pinchanx, Y. Petroff, and L. M. Falicov, Phys. Rev. Lett. **39**, 1632 (1977).
[2] G. G. Tibbets and W. F. Egelhoff, Phys. Rev. Lett. **41**, 188 (1978).
[3] D. R. Penn, Phys. Rev. Lett. **42**, 921 (1979).
[4] L. A. Feldkalm and L. C. Davis, Phys. Rev. Lett. **43**, 151 (1979); J. Appl. Phys. **50**, 1944 (1979).
[5] S. Huefner and G. K. Wertheim, Phys. Lett. **51A**, 299 (1975).
[6] R. Bruhn, S. Sonntag, and H. W. Wolff, J. Phys. B **12**, 203 (1979).
[7] E. J. McGuire, Phys. Rev. A **5**, 1052 (1972).
[8] M. Iwan, F. J. Himpsel, and D. E. Eastman, Phys. Rev. Lett. **43**, 1829 (1979).
[9] M. Iwan, E. E. Koch, T. C. Chiang, D. E. Eastman, and F. J. Himpsel, Solid State Commun. **34**, 57 (1980).
[10] D. Chandesris, C. Guillot, G. Chauvin, J. Lecante, and Y. Petroff, Phys. Rev. Lett. **47**, 1273 (1981).
[11] R. Bruhn, E. Schmidt, H. Schroder, and B. Sonntag, J. Phys. B **15**, L441 (1982).
[12] L. C. Davis and L. A. Feldkamp, Phys. Rev. Lett. **44**, 673 (1980).
[13] S. M. Givin and D. R. Penn, Phys. Rev. B **22**, 4081 (1980).
[14] L. C. Davis and L. A. Feldkamp, Phys. Rev. B **23**, 6239 (1981).
[15] L. C. Davis and L. A. Feldkamp, Phys. Rev. A **24**, 1862 (1981).
[16] L. J. Garvin, B. R. Brown, S. L. Carter, and H. P. Kelly, J. Phys. B **16**, L269 (1983); J. C. Chang (unpublished).
[17] J. C. Chang (unpublished).
[18] Z. Altum and H. P. Kelly, Phys. Rev. A **31**, 3711 (1985).
[19] L. J. Garvin, B. R. Brown, S. L. Carter, and H. P. Kelly, J. Phys. B **16**, L643 (1983).
[20] W. Wijeundera and H. P. Kelly, Phys. Rev. A **36**, 4539 (1987); Phys. Rev. A **39**, 634 (1989).
[21] B. R. Brown, S. L. Carter, and H. P. Kelly, Phys. Rev. A **21**, 1237 (1980).
[22] A. F. Starace, in *Theory of Atomic Photoionization,* edited by S. Flugge and W. Mehlhorn, Handbuch der Physik, Vol. XXXI (Springer-Verlag, Berlin, 1982), p. 1.
[23] U. Fano and J. W. Copper, Rev. Mod. Phys. **40**, 411 (1968).
[24] K. A. Brueckner, Phys. Rev. **97**, 1353 (1955).
[25] H. P. Kelly, Adv. Theor. Phys. **2**, 75 (1968).
[26] H. P. Kelly, in *Photoionization and Other Problems of Many-Electron Interaction,* edited by F. Wuilleumier (Plenum, New York, 1976), p. 83.
[27] L. M. Frantz, R. L. Mills, R. G. Newton, and A. M. Sessler, Phys. Rev. Lett. **1**, 340 (1958); H. J. Silverstone and M. L. Yin, J. Chem. Phys. **49**, 2026 (1968).
[28] C. Froese Fischer, Comput. Phys. Commun. **14**, 145 (1978).
[29] U. Fano, Phys. Rev. **124**, 1866 (1961).
[30] E. J. McGuire, Phys. Rev. A **5**, 1052 (1972); J. Phys. Chem. Solid **33**, 577 (1972).
[31] C. E. Moore, *Atomic Energy Levels,* Natl. Bur. Stand. (U.S.) Circ. No. 467 (U.S. GPO, Washington, DC, 1971), Vol. II.